

Laser powder bed fusion of a Fe–Mn–Si shape memory alloy

I. Ferretto^a, D. Kim^b, N.M. Della Ventura^a, M. Shahverdi^a, W. Lee^b, C. Leinenbach^{a,*}

^a Empa, Swiss Federal Laboratories for Materials Science and Technology, 8600 Dübendorf, Switzerland

^b Dongnam division, Korea Institute of Industrial Technology, 50623 Yangsan, Republic of Korea

ARTICLE INFO

Keywords:

Laser powder bed fusion
Texture
Microstructure
Shape memory alloys
Shape memory effect

ABSTRACT

The iron-based Fe–17Mn–5Si–10Cr–4Ni shape memory alloy (SMA) has been manufactured by laser powder bed fusion (LPBF) for the first time. High strength, elongation and ductility are observed after annealing. In addition, pronounced shape memory effect (SME) and pseudo-elasticity (PE), which exceed those measured for the conventionally fabricated Fe–17Mn–5Si–10Cr–4Ni–1(V,C) alloy containing VC precipitates, are achieved.

The texture generated during the LPBF process brings to SME and PE highly dependent on the orientation of the loading direction with respect to the build direction. Improved strain recovery is observed when the loading direction is parallel to the build direction due to an increased amount of (101) orientated grains with high Schmid factor and low yield strength for phase transformation.

Pronounced shape recovery is also obtained in more complex geometries successfully fabricated with the same manufacturing technique.

1. Introduction

Shape memory alloys (SMAs) are materials characterized by a shape memory effect (SME) and pseudo-elasticity (PE). The SME occurs when a deformed material can recover the original shape upon heating. PE describes the recovery of a large nonlinear elastic strain upon loading and unloading [1]. The unique effects observed in these materials are the results of a diffusion-less solid-state phase transformation (the martensitic transformation) between a high temperature phase, the parent phase or austenitic phase, and a low temperature phase, the martensitic phase [1,2].

SME was first found in Au–Cd alloy by Chang and Read in 1951 [3] and some years later (1963) in a Ni–Ti alloy by Buehler et al. [4]. Since then, Ni–Ti SMAs have been widely investigated. Due to the combination of high SME, low modulus of elasticity, and biocompatibility [5], they hold the first position in the industrial market [2]. SMAs show great potential for actuators in the biomedical and aerospace fields or even for tensioning and damping structures in buildings [6]. However, the high cost of raw material and processing of Ni–Ti alloys represents the main drawback of this class of materials [7] and limits its applications in civil and structural engineering, where a large amount of material is required for big size structures subjected to relatively high forces [6]. In this scenario, Fe–Mn–Si–X alloys represent potential low cost materials for large-scale applications in civil and structural engineering [8,9]. The

cost of Fe-based SMAs is estimated to be a small fraction of the Ni–Ti alloys [6]. The first Fe–Mn–Si alloy exhibiting SME was examined by Sato in 1982 [10]. Subsequently, cost-saving Fe–Mn–Si SMAs characterized by good mechanical property and machinability have been developed and applied in civil engineering structures. At Empa, a novel Fe–Mn–Si–Cr–Ni–(V,C) alloy with high recovery stress and great mechanical and corrosion properties was developed and applied to pre-stress concrete structures [11,12]. The effect of precipitates, texture, grain size [13] and grain orientation [14,15] on the martensitic transformation, as well as the alloy response under cyclic mechanical loading, creep and stress relaxation behavior [7] have been widely analyzed.

Until now, many studies have been carried out for Fe–Mn–Si alloys produced by melting and casting in high vacuum or high purity shielding gas facilities [16]. Additional machining, i.e. hot-forging and cold-rolling, is usually required in order to obtain the final shape, limiting the production to components with simple geometries, e.g. strips or bars. Additive manufacturing (AM) technologies such as Laser Powder Bed Fusion (LPBF) could open new perspectives to overcome the constraints of conventional manufacturing in terms of complexity and to fully exploit the attractive functionalities of these SMAs. Indeed, the full melting of the raw metal powder during AM enables the generation of intricate parts and fully dense highly specialized components within a single production step [17].

LPBF of Ni–Ti alloys has been widely examined in the recent years. A

* Corresponding author.

E-mail address: christian.leinenbach@empa.ch (C. Leinenbach).

<https://doi.org/10.1016/j.addma.2021.102071>

Received 5 March 2021; Received in revised form 19 May 2021; Accepted 20 May 2021

Available online 6 June 2021

2214-8604/© 2021 The Author(s). Published by Elsevier B.V. This is an open access article under the CC BY-NC-ND license

(<http://creativecommons.org/licenses/by-nc-nd/4.0/>).

summary of the investigations and discoveries can be found in the review papers of Elahinia et al. [18], Van Humbeek [19] or Chekotu et al. [20]. According to these studies, LPBF of Ni–Ti alloys is rather challenging. The cyclic heating and cooling during the process is associated with changes in the alloy chemistry and with the formation of special/characteristic microstructures, which can affect the shape memory behavior [21,22]. It is known that small variations in the chemical composition (e.g. by 0.1 at.%) can induce alterations of the phase transformation temperatures of Ni–Ti alloys by approximately 10 K [23]. Furthermore, modifications of the processing parameters can lead to pronounced variations of material texture and microstructure, strongly influencing the shape memory characteristics [24].

AM of Fe-based SMAs has been only scarcely studied until now. The fabrication of a Fe–Mn–Al–Ni alloy with good PE by LPBF was demonstrated by Niendorf et al. [25]. However, the alloy is prone to cracking during LPBF, and preheating at 500 °C is required to fabricate crack-free samples [26]. To the authors' best knowledge, Fe–Mn–Si alloys have been only applied in laser cladding experiments [27,28] but no research on AM has been conducted so far. Most of the works on Fe–Mn–Si SMAs focus on microstructural and thermo-mechanical properties of conventionally produced parts. LPBF is expected to lead to different microstructures and textures and thereafter to different shape memory properties.

The main objective of this work is to demonstrate the feasibility of printing bulk parts exhibiting SME and PE from a previously studied Fe–Mn–Si SMA. Fundamentals on process-microstructure-property relationships governing the AM manufactured alloy are provided by a detailed thermo-mechanical and microstructural characterization. The shape memory properties of the LPBF fabricated samples are compared with the performance of previously conventionally produced specimens to ascertain the applicability of this innovative technique as a valid alternative to standard processing routes. In addition, the SMA integration by LPBF into more complex and compliant 3D geometries exhibiting pronounced shape recovery is also demonstrated to point out the high flexibility and design freedom, which characterize LPBF.

The present study represents the starting point for enlarging the fabrication of Fe-based SMAs by AM, opening a new window for developing innovative functional materials, which combine shape memory properties with enhanced functionalities, such as damping capacities or high-energy absorption, deriving from intricate and compliant geometries.

2. Materials and methods

2.1. Powder

In this work, a Fe-based SMA with the nominal composition Fe–17Mn–5Si–10Cr–4Ni (wt%) was used as testing material. The powder was produced by gas atomization in Argon atmosphere (Metal Player Co., Ltd., Republic of Korea) and has a chemical composition similar to the one of the SMA investigated in a previous study [15], but does not contain V and C. The composition as provided by the powder supplier is given in Table 1. Most of the powder particles were found to be spherical, with a d_{50} of 29.7 μm and a size distribution ranging from 10 to 50 μm (Figs. A1, 2 in Appendix A).

2.2. Sample preparation

2.2.1. Sample geometries and LPBF processing parameters

In order to optimize the LPBF parameters, cubes of 10×10×10 mm³

were fabricated with different laser parameters for microstructure investigation and defect analysis. The specimens were manufactured in an Argon environment (less than 0.1% Oxygen content) using a Sisma MySint 100 (Sisma S.p.A., Italy) operating in continuous mode with a 200 W 1070 nm fiber-laser and a Gaussian intensity distribution (55 μm spot size). A bidirectional scanning strategy with a 90° rotation between layers and border contour was applied for all the samples. Hatch spacing (h) and layer thickness (t) were kept constant at 0.1 mm and 0.03 mm, respectively. The machine operated with power (P) ranging from 115 to 175 W and scanning speed (v) from 300 to 600 mm/s, so that the volumetric energy density (VED), defined as

$$\text{VED} = \frac{P}{h \cdot t \cdot v} \quad (1)$$

ranges from 63.89 to 194.44 J/mm³. The processing parameters are summarized in Table A 1 of Appendix A.

The optimized processing parameters, with which high densities and minimal defects could be achieved, were applied to produce tensile specimens. The initial blocks were fabricated from the same powder using the highest VED (VED=194.44 J/mm³), i.e. P of 175 W and v of 300 mm/s. Dog-bone tensile samples were prepared using electro discharge machining from each block in two series, differing in orientation of their loading direction with respect to the build direction. Batch H (horizontal samples) has loading direction normal to the build direction and batch V (vertical samples) has loading direction parallel to build direction (Fig. 1).

2.2.2. Heat treatments

The aforementioned cubes and blocks used for tensile specimens and manufactured with the highest VED were heat treated after printing. Since the SME is caused by the fcc- $\gamma \rightarrow$ hcp- ϵ transformation and its reversion, annealing heat treatment at 800 °C for 30 min was performed in order to obtain an austenitic microstructure (fcc- γ) and dissolve any ferritic phase (bcc- δ) resulting from the rapid consolidation.

2.3. Sample characterization

2.3.1. Sample density and defects

The density of the cubes was determined using the Archimedes' method with a Mettler Toledo XS205DU density meter with an accuracy of $\pm 0.0005 \text{ g/cm}^3$. The absolute densities were determined by measuring the weight of the samples in air and in high purity ethanol at room temperature. The relative densities were determined considering a theoretical density of the alloy of 7.491 g/cm³, which was calculated using ThermoCalc 2021b in combination with the TCFE-7 database.

The cubes were then sectioned parallel to the build direction for cross section investigations. The samples were cold-mounted in epoxy, ground and polished. For the final polishing step, 50 nm colloidal silica was used. Pores, lack of fusion defects and cracks were characterized in the

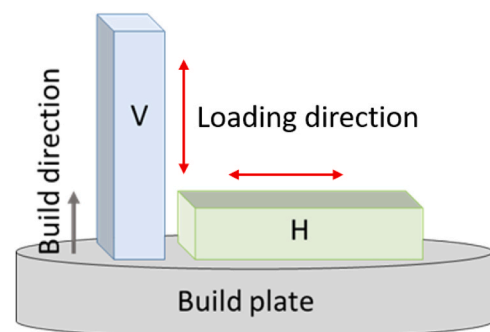


Fig. 1. Tensile specimens. Orientation of the loading direction (red arrow) with the build direction. (For interpretation of the references to color in this figure legend, the reader is referred to the web version of this article.)

Table 1

Powder chemical composition.

Fe (wt%)	Mn (wt%)	Cr (wt%)	Si (wt%)	Ni (wt%)
bal.	17.25	9.90	5.10	4.04

polished samples using optical microscopy (OM) with a Zeiss Axiovert 100A/Canon DSLR and scanning electron microscopy (SEM) with a FEI NanoSEM 230 equipped with a high-efficiency Oxford X-Max SDD EDX system. After grinding and polishing by standard metallographic techniques, the samples were etched using V2A etchant at room temperature (100 mL hydrochloric acid, 100 mL water, 10 mL nitric acid) and analyzed by SEM. The chemical composition of selected samples after LPBF was determined by energy-dispersive X-ray (EDX).

2.3.2. Microstructure analysis and phase identification

In order to analyze the process of phase formation and transformation as a function of the process parameters, X-ray diffraction (XRD) was performed on a Bruker D8 using $\text{CuK}\alpha$ radiation. A pinhole of 1 mm diameter was used. Electron backscatter diffraction (EBSD) analysis was also conducted on a SEM Tescan Mira equipped with an EDAX DigiView camera. The electron beam voltage was set to 20 kV, the step size was $1\text{ }\mu\text{m}$ for $500 \times 500\text{ }\mu\text{m}^2$ maps. EBSD analysis was applied to investigate the phase formation and distribution, grain size, grain orientation and texture in samples manufactured with different processing conditions. XRD and EBSD measurements were performed on the cross sections of the cubic samples in the as-built condition and after heat treatment. Moreover, sections of the gauge length were cut out of the un-deformed tensile samples (both V and H batches) and one side, parallel to the loading direction, were ground and polished as described above. EBSD characterization was conducted also on these surfaces in order to assess the grain orientation along the loading direction. The acquired EBSD data were processed with EDAX OIM Analysis 7.3 software.

2.3.3. Thermo-mechanical characterization

The heat treated tensile specimens were tested with regard to their thermo-mechanical properties. Samples from batch V and batch H were analyzed. For each condition, at least two samples were tested. Yield strength ($\sigma_{y0.2}$), ultimate tensile stress (UTS) and elongation to fracture were characterized by a strain controlled tensile test until failure in a Zwick/Roell Z020 tensile testing machine at room temperature. The tensile sample gauge measures 1.6 mm and 1.5 mm in width and thickness and 32 mm in length (Fig. 2).

The same tensile machine was used for cyclic strain-controlled loading and unloading in order to characterize material's PE as described in the previous work [7]. The samples were cyclically loaded and unloaded to a holding force of 10 N. In the first cycle, 1% strain was reached before unloading. In the subsequent cycles, the strain was increased stepwise by 1% every cycle, until a maximum strain of 10%. For each cycle, the pseudo-elastic strain (ϵ_{pse}) was determined by the difference of the hypothetic strain upon linear unloading and the experimentally measured strain upon unloading. In order to characterize and compare the PE of the two V and H batches, for every cycle of the curves ϵ_{pse} and hysteresis opening (ϵ_{hyst}), i.e. the half width of the

hysteresis loop at mean stress, were measured and reported as function of the applied stress.

In order to characterize the SME, experiments were performed in a climate chamber attached to the Zwick/Roell Z020 tensile testing machine and equipped with an electrical heating and cooling system. The strain evolution was recorded with a clip-on extensometer tied with a thermocouple to measure its temperature during the tests. The error deriving from the extensometer thermal expansion could be calculated and compensated accordingly. The tensile samples were pre-strained to 4% at room temperature and then unloaded under strain-controlled conditions with a deformation rate of 0.2 mm/min. The pre-strained samples were then fixed at both ends and subjected to a very small preload (10 N). Keeping this preload constant, heating to 200 °C and cooling to room temperature were performed at a rate of 2 °C/min. The temperature was kept constant for 30 min when the maximum temperature and room temperature were reached in order to ensure a homogenous temperature distribution within the samples. The final strain measured by the extensometer at the end of the thermal cycle was reported as recovery strain.

2.4. Demonstration of complex 3D structure fabrication by LPBF

The possibility of fabricating complex-shaped parts with the investigated Fe–Mn–Si SMA using LPBF was also demonstrated. Several objects were designed using the commercial computer-aided design software Autodesk Inventor (Autodesk, Mill Valley, CA, USA) and are shown in Fig. 3. The fabrication of the objects was conducted using a second LPBF system, the OPM250L (Sodick Co., Ltd., Japan), equipped with a 500 W Yb-YAG laser (1070 nm) with a Gaussian beam distribution and a spot size of 200 μm . Because of the different laser properties, the processing parameters had to be adjusted in order to minimize defects and undesired phase formation, e.g. bcc- δ phase, in the as-built state. The LPBF parameters used to produce the objects are listed in Table 2. The printed objects were cut from the base plate and then heat treated at 800 °C for 30 min.

The fabricated objects were deformed at room temperature and heated by a heat gun with a set temperature of 300 °C in order to activate the SME and demonstrate the possibility of shape recovery also in more complex geometries.

3. Results

3.1. Sample density and defects

Fig. 4-a displays the measured relative densities as a function of the VED for three different scanning speeds, showing a decrease of relative density with a reduction of VED. According to Fig. 4b, scanning speed has much more influence on specimen's densification. Three samples were tested for every parameter combination, and only a slight sample-by-sample variation was observed. To reach highly dense parts, a low scanning speed has to be applied. A pronounced increase in density is observed by decreasing the scanning speed to the minimum value (300 mm/s), for which a maximum value of approximately 99.8% could be achieved with a laser power of 175 W. The impact of laser power on the material's density becomes significant only at low (300 mm/s) and high (600 mm/s) scanning speeds. While an increase in density is observed by increasing the power for 300 and 600 mm/s scanning speed, almost no variation in the material's density with laser power is observed when the scanning speed is equal to 450 mm/s. Additionally, samples fabricated with the same VED but obtained by different parameter combinations do not show the same density.

Binding or lack of fusion defects, as well as contour defects, form at $\text{VEDs} < 161.11\text{ J/mm}^3$. The samples are characterized by elongated voids with equivalent diameter larger than 30 μm and with sharp edges (Fig. 5-a,c). Long horizontal cracks are also observed on the samples manufactured at $\text{VEDs} < 144.44\text{ J/mm}^3$ (Fig. 5-c). By increasing the

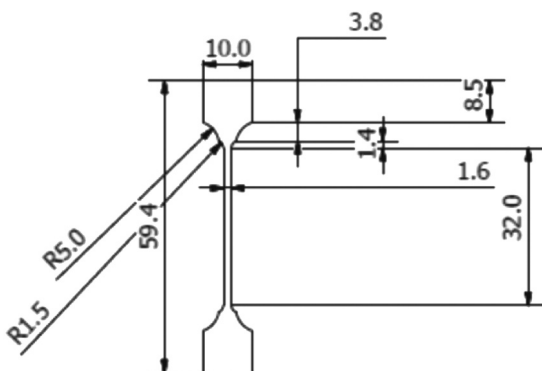


Fig. 2. Dog-bone sample geometry, dimensions in mm.

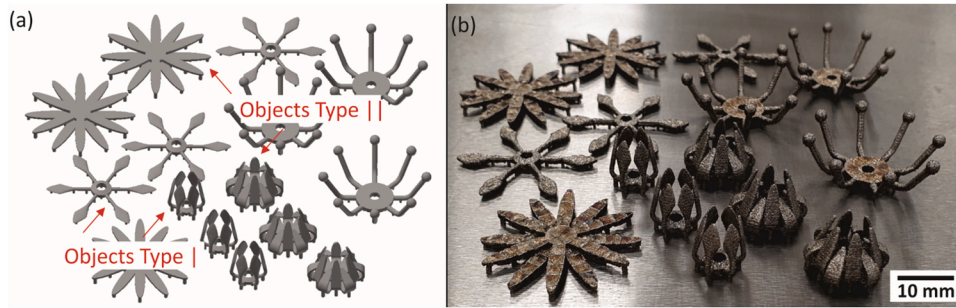


Fig. 3. (a) Computer-aided design data for 3D objects; (b) as-printed objects.

Table 2

LPBF parameters used for Sodick OPM250L machine.

Power (P)	Scanning speed (v)	Hatch spacing (h)	Layer thickness (t)	Vol. energy density (VED)
420 W	800 mm/s	0.1 mm	0.05 mm	105 J/mm ³

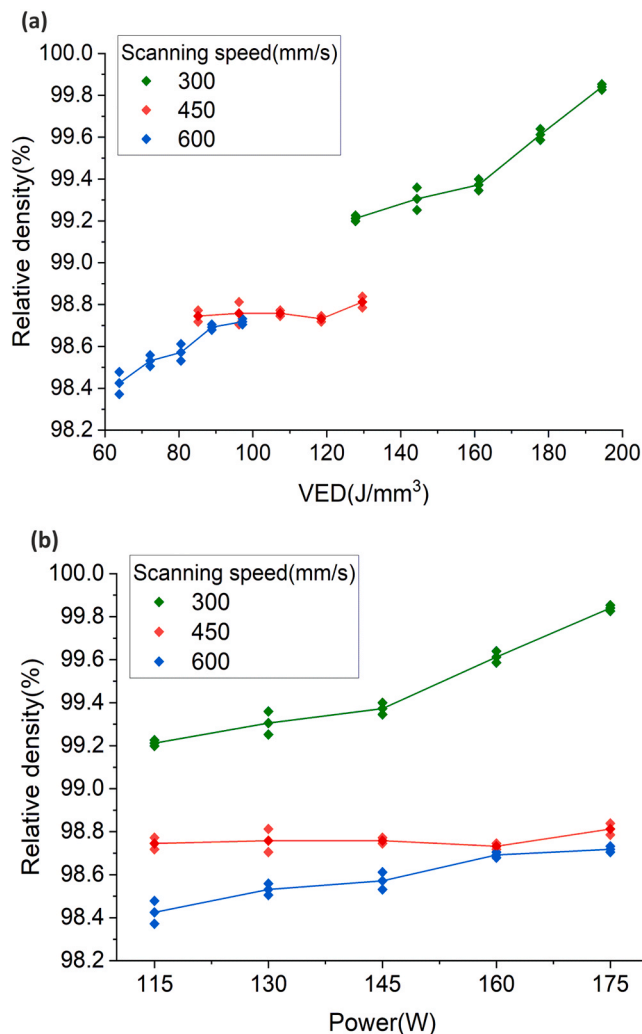


Fig. 4. (a) Variation of relative density with VED; (b) Variation of relative density with laser power.

VED, the formation of these types of defects is prevented and almost fully dense parts are fabricated. Only a few spherical pores, probably due to the presence of porosity in the powder, are observed (Fig. 5b,d).

In Fig. 5, OM and SEM images of samples fabricated with the lowest (63.89 J/mm³) and highest (194.44 J/mm³) VED are displayed for comparison. Given the results summarized in Fig. 4 and Fig. 5, samples manufactured with the maximum VED of 194.44 J/mm³ seem to provide the best condition in terms of part densification and defect formation.

Additional EDX measurements suggest that the amount of Mn is decreased by approximately 0.5% after LPBF, while the amount of the other alloying elements remains almost unchanged.

3.2. Microstructure analysis and phase identification

The color contrast observed in OM images in Fig. 5c,d indicates the formation of different phases within the samples, which are identified as bcc- δ (darker phase) and fcc- γ (brighter phase) by XRD and EBSD analysis. The XRD patterns (Fig. 6) taken from the samples fabricated with the maximum (194.44 J/mm³) and the minimum VED (63.89 J/mm³) denote that the VED strongly influences the phase formation and distribution within the as-built parts. The sample fabricated with a VED of 194.44 J/mm³ shows an almost fully austenitic microstructure (fcc- γ). A weak peak of hcp- ϵ is also detected, although no mechanical loading has been applied. One possible reason for the formation of hcp- ϵ could be the accommodation of residual stresses, which formed during the process. In contrast, bcc- δ is the predominant phase detected in the lowest-VED sample. The amount of bcc- δ is around 98% according to EBSD measurements, significantly higher when compared with the highest-VED sample (13%).

Variations in grain size, orientation and morphology are also observed by comparing the EBSD maps in Fig. 7a,b, as well as the SEM images in Fig. 5-a,b. Nearly vertically oriented columnar grains of bcc- δ form in the lowest-VED sample. The majority of the grains are characterized by a high aspect ratio, with the largest dimension of several dozens of micrometers in the build direction. The weighted average of grain dimension is around 60 μ m. Ferritic grains show a pronounced $\langle 001 \rangle$ orientation along the build direction (Fig. 7-a,c).

At the maximum VED, the microstructure is mainly composed of fine equiaxed grains, with diameters below 10 μ m. Slightly elongated grains along the build direction are detected only in a few regions. A change in grain orientation is also observed by analyzing the inverse pole figure map and the inverse pole figures of an almost fully austenitic region. The fcc- γ grains show a preferred $\langle 101 \rangle$ alignment with the build direction (Fig. 7b,d).

Heat treatment of the samples fabricated with the highest VED leads to the complete dissolution of the bcc- δ phase. Significant grain growth during the heat treatment is not observed (Fig. 8a). The average grain size after heat treatment is around 10 μ m. In Fig. A 3 of Appendix A the grain size distributions for the maximum-VED samples in as-built and heat treated condition are reported for comparison. As in the as-built part, inverse pole figures and inverse pole figure map depict a strong $\langle 101 \rangle$ orientation of the austenitic grains with the build direction (Fig. 8-a,b) and $\langle 001 \rangle$ with one of the two scan directions.

The tensile samples after annealing were also investigated by EBSD. The inverse pole figures reported in Fig. A4 in Appendix A show grains

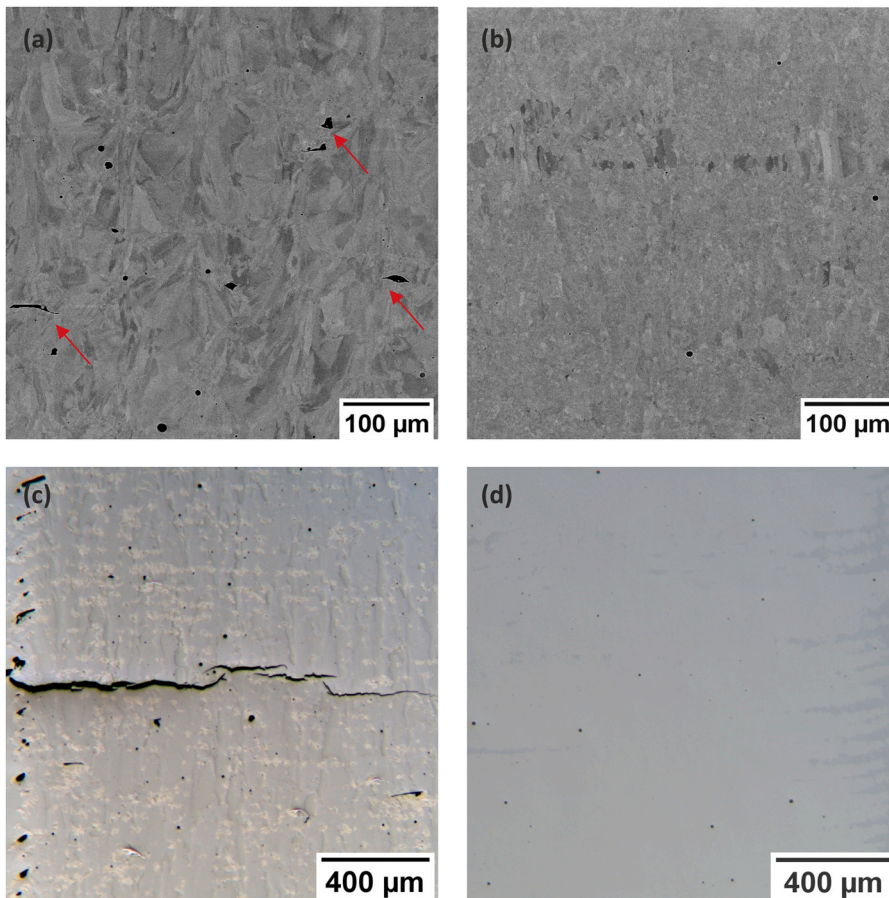


Fig. 5. (a) SEM image of the cross section of the sample fabricated with the lowest VED showing lack of fusion defect formation (red arrows); (b) SEM image of the cross section of the sample fabricated with the highest VED; (c) OM image of the cross section of the sample fabricated with the lowest VED, showing formation of contour defects and cracks; (d) OM image of the cross section of the sample fabricated with the highest VED. (For interpretation of the references to color in this figure legend, the reader is referred to the web version of this article.)

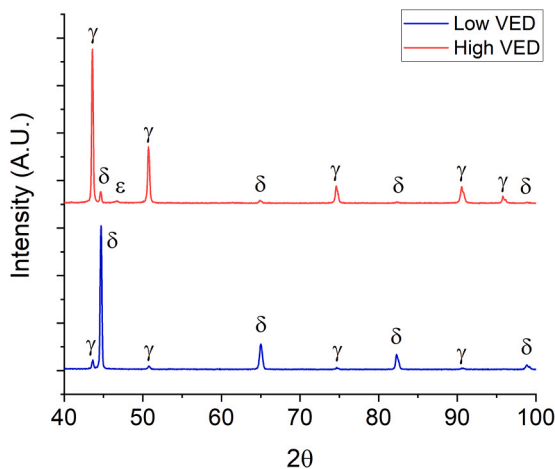


Fig. 6. XRD patterns of the samples manufactured with the maximum (194.44 J/mm^3) (red) and minimum (63.89 J/mm^3) (blue) VED. (For interpretation of the references to color in this figure legend, the reader is referred to the web version of this article.)

with strong $\langle 101 \rangle$ orientation for vertical samples, and grains with pronounced $\langle 001 \rangle$ orientation for horizontal samples along the loading direction. This is in line with the observed texture of the cubic samples, considering that the loading direction corresponds to the build direction in vertical specimens and with the scanning direction in the horizontal ones.

3.3. Thermo-mechanical characterization

3.3.1. Stress-strain behavior

Fig. 9a shows monotonic stress-strain curves until fracture obtained for a sample with the loading direction parallel (vertical sample, batch V) to the build direction and for a second sample with the loading direction along the scan direction, i.e. perpendicular to the build direction (horizontal sample, batch H) after annealing at 800°C . For the sake of clarity, only a single representative curve for each tested condition is shown.

The curves first follow a linear elastic behavior and then deviate non-linearly due to a combination of martensitic transformation and plastic flow [29]. Table 3 lists the standard mechanical properties. The standard 0.2% yield strength does not reflect exactly the starting point of the non-linearity behavior because of the stress-induced martensite (hcp- ϵ) formation [7]. The stress at which the stress-strain curves deviate from the linear behavior is measured and defined as the critical stress to induce martensite formation. Lower stress values are required for the vertical samples ($\sim 167 \text{ MPa}$) than for the horizontal ones ($\sim 195 \text{ MPa}$).

High elongations are measured for the two batches, with horizontal samples showing lower values (34.11% vs. 47.86%) but higher strength (UTS of 940.67 MPa) with respect to the vertical ones (UTS of 882.42 MPa). More pronounced hardening is observed for the horizontal samples. The fracture surfaces of both vertical and horizontal samples present the characteristic dimple topography, indicating a ductile fracture mode Fig. 9-b).

3.3.2. Pseudo-elasticity

Fig. 10a displays the loading and unloading cycles for the vertical and horizontal samples. In every cycle, the curves do not follow a linear trend during unloading and hysteresis loops are observed (Fig. 10a).

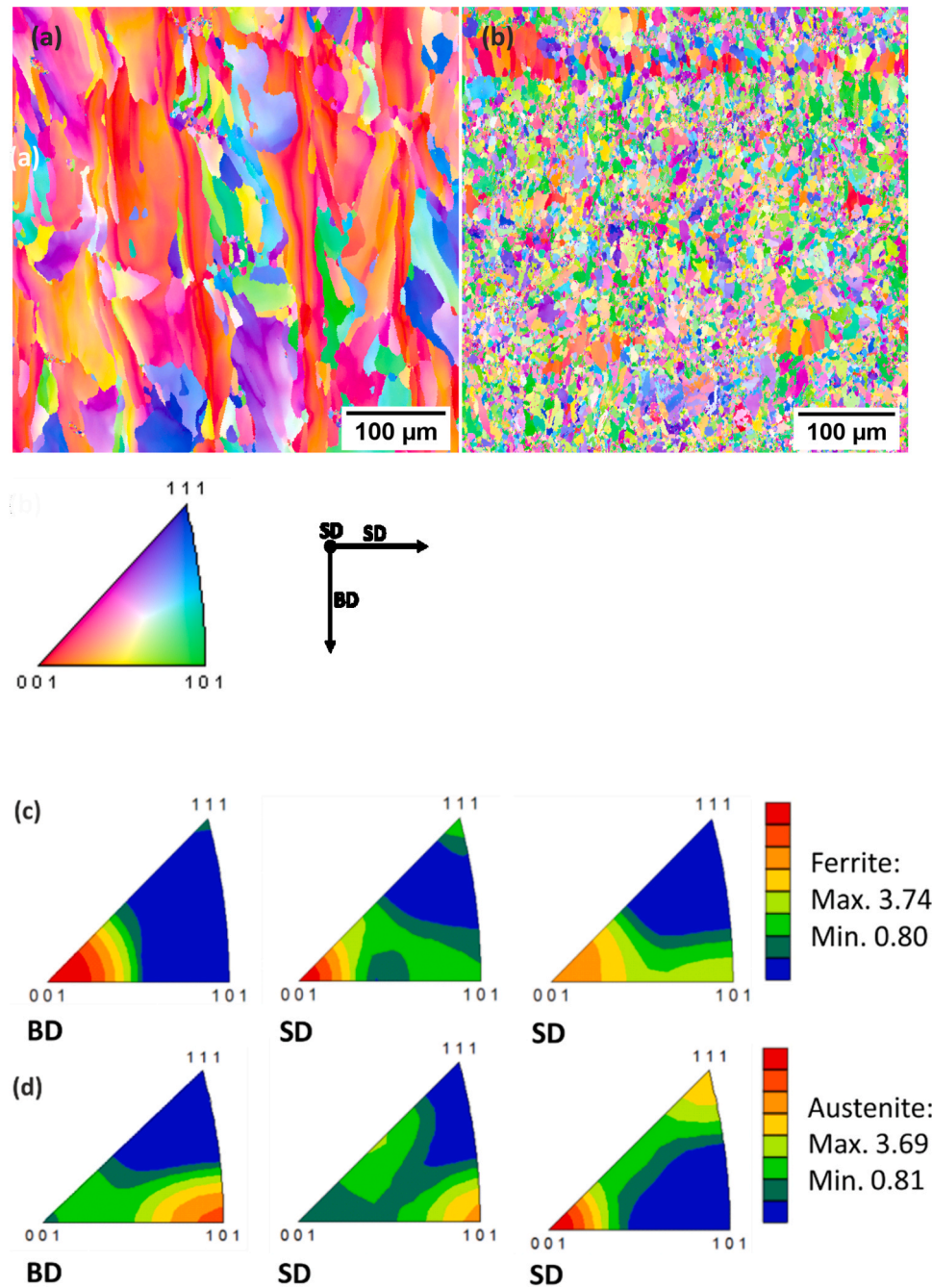


Fig. 7. EBSD analysis; inverse pole figure map related to the build direction (BD in the picture) of as-built samples fabricated with (a) the lowest-VED and (b) the highest-VED; inverse pole figures for the build direction (BD) and for the two scan directions (SD) of the as-built samples fabricated with (c) the lowest-VED and (d) the highest-VED.

This deviation of the curve behavior from Hook's law reveals a partial strain recovery due to the material's PE. The non-linear recovered strain is associated with a back transformation to fcc- γ of the martensitic phase induced during the stress application [13]. For an equal stress level, higher ϵ_{pse} and ϵ_{hyst} are measured for the vertical samples than for the horizontal ones (Fig. 10b). For both batches, an increase in ϵ_{pse} and ϵ_{hyst} with the stress applied during loading is observed. At the higher stresses, ϵ_{hyst} exceeds 1% and asymptotically approaches a value of approximately 1.3%.

3.3.3. Shape memory effect

Fig. 11 shows the recovered strain of the tensile samples (batches V and H) elongated to 4% total strain as a function of temperature during

heating to 200 °C and subsequent cooling. The recovery strain curves can be divided into two branches. In the first branch (heating to 200 °C), a back transformation from the stress-induced hcp- ϵ to fcc- γ occurs together with the sample thermal expansion. A large amount of back transformation is required to achieve a large recovery strain (compressive strain) and overcome the thermal expansion effect. In the second branch, the material is cooled down. No further transformation from hcp- ϵ to fcc- γ takes place and any further deformation of the samples is only related to the thermal contraction.

For both the batches, a net sample contraction is achieved during heating due to a pronounced strain recovery that dominates over the thermal expansion. Specimen contraction starts at a slightly lower temperature (~ 47 °C) in vertical samples than in horizontal samples

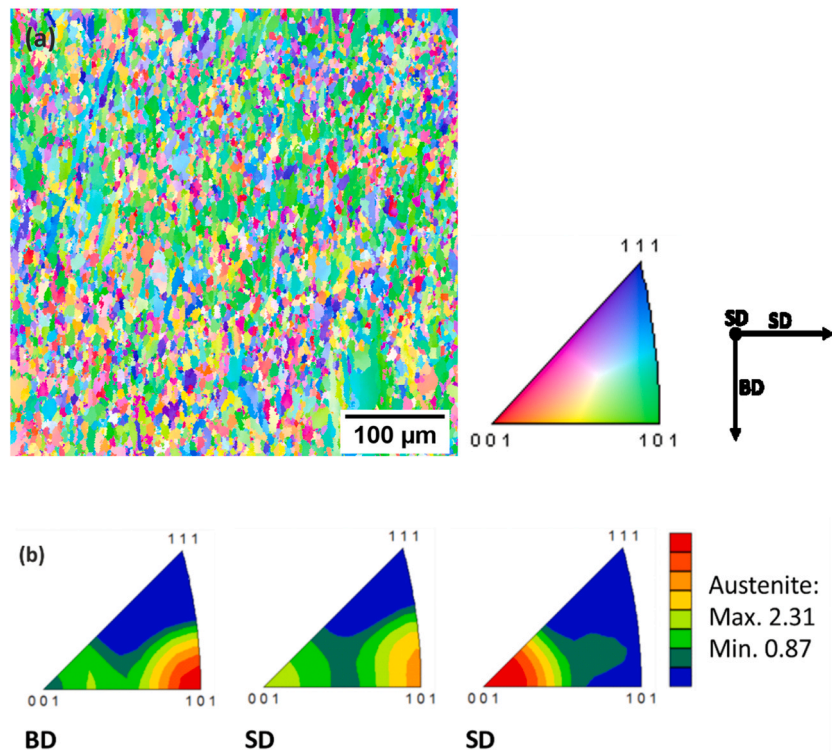


Fig. 8. EBSD analysis; (a) inverse pole figure map and (b) inverse pole figures for sample fabricated at the highest VED after heat treatment at 800 °C for 0.5 h.

(~59 °C) and reaches higher values at 200 °C (1.36% vs. 1.02%), as well as at room temperature (1.64% vs. 1.29%), indicating superior SME for the former. Therefore, an orientation vertical to the build direction is preferable to achieve a more pronounced SME.

4. Discussion

4.1. Sample density and defects

Parts built with low VED suffer from poor density due to the formation of defects during the fabrication. The insufficient melting of the powder and the inadequate penetration of the melt pool into the previous deposited layers [30] lead to a lack of bonding between tracks and layers, and, consequently, to the generation of the observed voids. Below a certain VED value ($<144.44 \text{ J/mm}^3$), cracking also occurs. The main reason for crack formation is the high amount of bcc- δ phase, which is particularly brittle compared to fcc- γ , in combination with the surface roughness and the residual stress associated with the high thermal gradient around the laser spot [31,32]. Indeed, cracks initiate and propagate at the edge of the samples where the surface roughness act as a source of stress concentration (notch effect) and residual stresses are particularly high.

In contrast, the high ratio of laser power to scanning speed applied for high-VED samples leads to increased melt pool size and penetration depth and ensures a reduction of molten material viscosity. Good bonding among tracks together with adequate wetting, spreading, flattening characteristics of the molten tracks are favored during deposition, guaranteeing the fabrication of dense bulk parts [32]. Considering the higher ductility of fcc- γ than bcc- δ , the mainly austenitic microstructure prevents cracking phenomena.

4.2. Microstructure analysis and phase identification

The samples fabricated at low VEDs show an increased amount of bcc- δ in comparison with the samples fabricated at high VEDs. It is known that austenitic stainless steels solidify as bcc- δ when the ratio

between the chromium equivalent, Cr_{eq} , and the nickel equivalent, Ni_{eq} , is greater than 1.5 [33]. There is a number of approaches for estimating the Cr_{eq} and Ni_{eq} in stainless steels. However, for Fe-Mn-Si SMAs they are usually calculated according to Hammar and Svensson [34].

$$\text{Cr}_{\text{eq}} = \% \text{Cr} + 1.5\% \text{Si} \quad (2)$$

$$\text{Ni}_{\text{eq}} = \% \text{Ni} + 0.31\% \text{Mn} + 22\% \text{C} \quad (3)$$

or according to Peng et al. [35].

$$\text{Cr}_{\text{eq}} = \% \text{Cr} + 1.5\% \text{Si} \quad (4)$$

$$\text{Ni}_{\text{eq}} = \% \text{Ni} + 0.164\% \text{Mn} + 22\% \text{C} \quad (5)$$

For the present alloy, values for $\frac{\text{Cr}_{\text{eq}}}{\text{Ni}_{\text{eq}}}$ of 1.708 and 2.271 are calculated respectively, suggesting that bcc- δ is the primary solidification phase.

In LPBF, the cooling rate during solidification in the melt pool as well as in the already solidified material is inversely proportional to the VED [36]. If the cooling rate is sufficiently low (i.e. at high VEDs), the primary phase, bcc- δ , transforms into fcc- γ in a solid-state transformation during cooling of the solidified layers. Heterogeneous nucleation of fcc- γ occurs at grain boundaries of the elongated bcc- δ grains. Austenitic grains can grow entirely across the ferritic grains, leading to the almost fully austenitic fine microstructure observed in high-VED samples (Fig. 12a,b). If the cooling rate exceeds a certain threshold value (i.e. at low VEDs), the formation of fcc- γ nuclei is largely suppressed and the bcc- δ grains, epitaxially grown as primary phase during deposition, are maintained at low temperatures after cooling.

The solid-state transformation bcc- $\delta \rightarrow$ fcc- γ is also responsible for the variation of the sample crystallographic texture with VED. Austenitic grains do not inherit the crystallographic orientation of the ferritic primary phase and are predominately $<101>$ oriented with regard to the build direction. While a fundamental study of the orientation relationship in the bcc- $\delta \rightarrow$ fcc- γ phase transformation and the resulting texture in the Fe-Mn-Si SMA is of academic interest, it is, however, beyond the

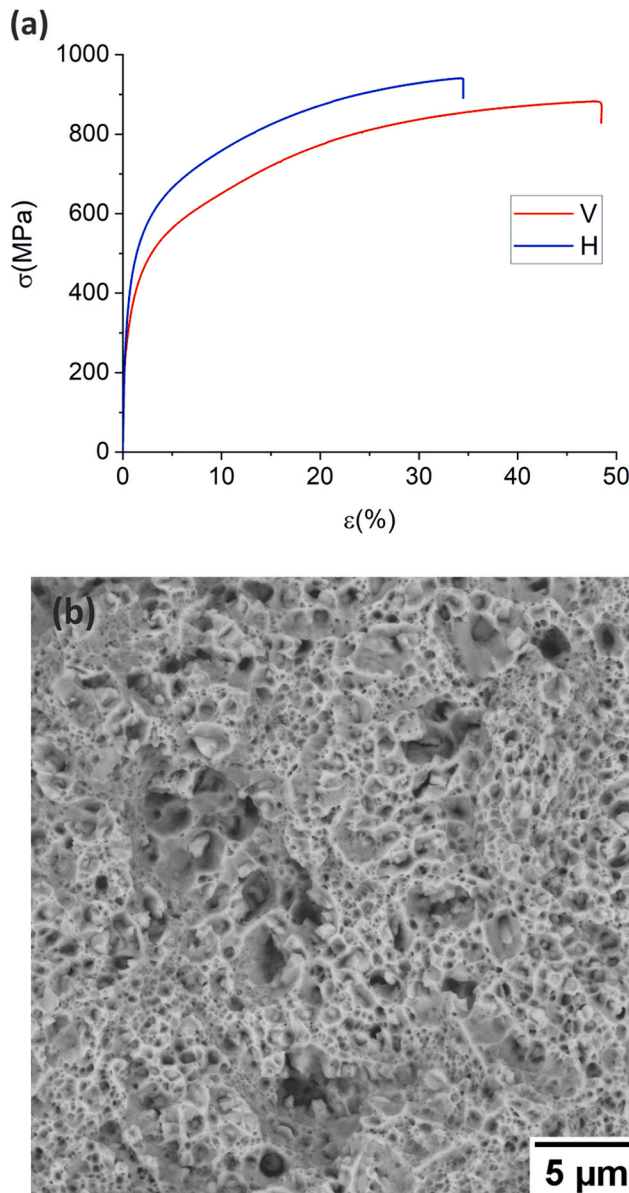


Fig. 9. (a) Representative stress-strain curves for horizontal and vertical samples; (b) SEM image of the ductile fracture features of one vertical sample after failure.

Table 3

Mechanical properties for the two batches of tensile specimens (horizontal, H and vertical, V).

Sample	$\sigma_{y0.2}$ (MPa)	UTS (MPa)	Elongation (%)
Horizontal	320.38	940.67	34.11
Vertical	278.73	882.42	47.86

scope of this work. Further investigations will be performed in future studies.

4.3. Thermo-mechanical characterization

4.3.1. Stress-strain behavior and pseudo-elasticity

A pronounced anisotropy in the stress-strain behavior is observed for the two batches V and H. The onset of non-linear deformation due to the martensitic transformation occurs at lower stress in samples with loading direction parallel to their build direction (batch V). This

difference is mainly attributed to the generated texture along the build direction, which results from the LPBF process. In a recent study, the grain orientation dependency of the phase transformation behavior from fcc- γ to hcp- ϵ of a precipitate containing Fe-17Mn-5Si-10Cr-4Ni-1(V,C) SMA was studied by in situ neutron diffraction and quasi-in situ EBSD [14]. The martensite formation and its reversion to austenite for individual grain families can be explained by considering the Schmid factors of the $\{111\} \langle 112 \rangle$ slip system involved in the fcc- γ to hcp- ϵ transformation. Upon the application of an external load, an increase in stacking fault width occurs for grain families whose Schmid factor of the leading partial dislocations (PDs) is higher than that of the trailing partial dislocations. According to the neutron diffraction study in Ref. [12], the (220) grains have leading PDs with a Schmid factor that is almost twice the one of trailing PDs. The opposite is observed for the (200) grains. As the stress-induced martensite formation proceeds by accumulation and overlapping of stacking faults, which nucleate on specific set of $\{111\}$ planes [37], the martensitic transformation is facilitated and required lower stress level in the vertical samples than in the horizontal ones. Indeed, the former exhibit an increased amount of (101) oriented grains along the loading direction, whereas the latter are characterized by a pronounced amount of (001) oriented grains. As a result, an early deviation from linearity of the stress-strain curve is observed for the V batch.

Since the strain recovery upon unloading, i.e. material's PE, is associated with the back transformation from hcp- ϵ to fcc- γ [14,15], and, therefore, with the amount of stress-induced martensite during loading, the variation in the stress required to induce martensite formation for the two fabrication conditions (batch H and batch V) has a direct impact on the specimen ϵ_{pse} . Specifically, the beginning of martensite formation at lower stress in the vertical samples than in the horizontal ones results in a lower stress required to induce PE. Furthermore, higher ϵ_{pse} is achieved in the former if the same stress is applied during loading due to a more pronounced martensite formation. The increase in ϵ_{pse} with increasing stress observed for both batches supports the hypothesis that PE is associated with the back transformation of the martensite accumulated during loading with the stress increase.

The positive impact of martensitic transformation on ductility has been widely investigated for a particular class of steels, defined as TRIP (Transformation induced plasticity) steels. The stress-induced martensite formation normally results in enhanced uniform elongation because of retardation of local necking [38]. Therefore, the more pronounced martensitic transformation for the V batch also brings to the superior elongation to fracture compared to the H batch.

4.3.2. Shape memory behavior

Similar to the stress-strain behavior, the SME is strongly affected by the sample orientation as a consequence of the different generated texture along the loading direction. The grain orientation dependency of the SME and the applicability of the Schmid law for alloys undergoing the martensitic transformation was already observed in a single crystal Fe-Mn-Si [39]. It was found that straining along the [011] direction, which shows low yield strength and high Schmid factor (0.47) for phase transformation, facilitates the martensitic transformation and brings to the formation of thin mono-partial hcp- ϵ plates [14,39]. Contrary, straining along the [001] direction, characterized by a low Schmid factor of 0.24 for phase transformation, creates martensitic variants on differently aligned planes. Moreover, the higher Schmid factor for irreversible slip (0.47) than for martensitic transformation indicates that plastic deformation is mainly governed by irreversible slip rather than by phase transformation.

According to Kajiwaru et al. [40], in addition to uniformly distributed stacking faults, the formation of thin plates of single variant martensite is an indispensable condition to achieve pronounced SME. Indeed, martensitic variants intersect each other, increasing the driving

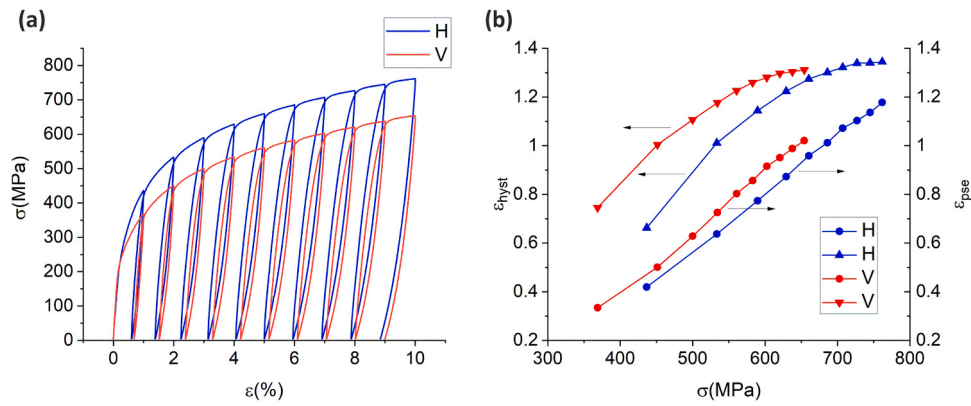


Fig. 10. (a) Cyclic loading-unloading curves for horizontal and vertical samples; (b) pseudo-elastic strain and hysteresis width as a function of the applied stress for horizontal and vertical samples.

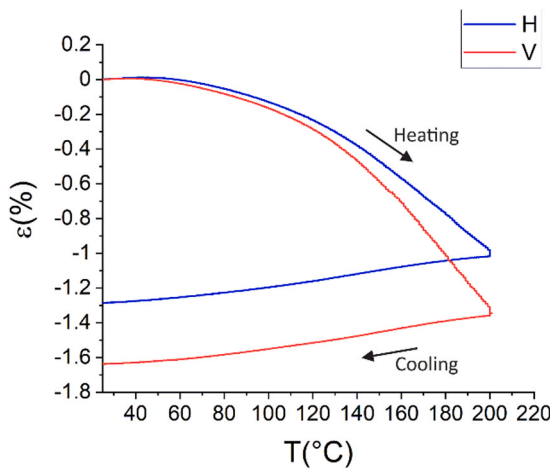


Fig. 11. Recovery strain of horizontal and vertical samples as a function of temperature after 4% pre-straining.

force to cause the back transformation to austenite upon heating. Considering that the loading direction of horizontal samples shows an increased amount of (001) grains, the low Schmid factor and the introduction of hcp- ϵ plates on different {111} planes are probably the reasons for the shift towards the higher temperature values required to induce the back transformation, and, consequently, for the inferior strain recovery. On the other hand, the interaction of slip and hcp- ϵ

bands and the interaction of different ϵ -hcp band variants lead to a more pronounced strain hardening effect and, hence, to the higher strength of the horizontal samples [39,41].

The improvement of the recovery strain upon unloading (PE) and heating (SME) was since ever part of the investigations of SMAs. For the Fe-Mn-Si alloy system, SME has been strongly improved by addition of 1 wt% of V and C to induce the formation of VC precipitates inside the grains after aging. The reason of this enhancement is ascribed to the generation of elastic strain fields around precipitates and to the formation of stacking faults, nucleation sites for the martensitic phase [18,20]. Moreover, precipitates increase the material's yield strength. Slip deformation is suppressed or retarded and plastic deformation is mainly governed by martensitic transformation rather than by irreversible slip. A decrease of the critical stress to induce hcp- ϵ formation is also observed in the presence of precipitates.

Conventionally manufactured specimens of the alloy Fe-17Mn-5Si-10Cr-4Ni-1(V,C) (i.e. with VC precipitates) exhibited a maximum ϵ_{pse} of 0.8% and a recovery strain of 1.15% [7,29]. The samples fabricated by LPBF in this work without V and C had higher values with a maximum ϵ_{pse} of 1.18% and recovery strain of up to 1.64%. One of the possible reasons for the enhanced performance of AM specimens is assumed to be the particular microstructure generated during the process. The high cooling rates and the cyclic heating and cooling experienced by LPBF samples lead to the formation of a complex microstructure in the final products, characterized by cellular structures of a few micrometers, which might affect the interaction between hcp- ϵ plates and the cell boundaries (Fig. 13). According to previous studies [41], grain boundaries exert back stresses on the dislocation involved in

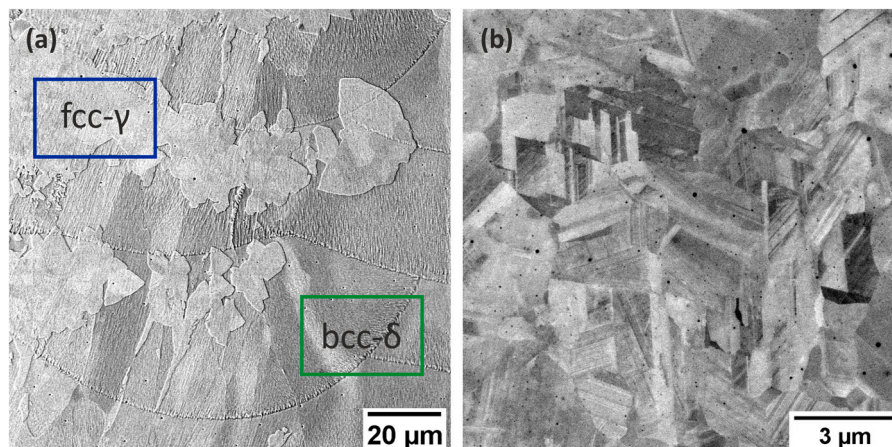


Fig. 12. (a) SEM image of fcc- γ formation from bcc- δ grains with the highest VED; (b) SEM image of the austenitic region at a higher magnification.

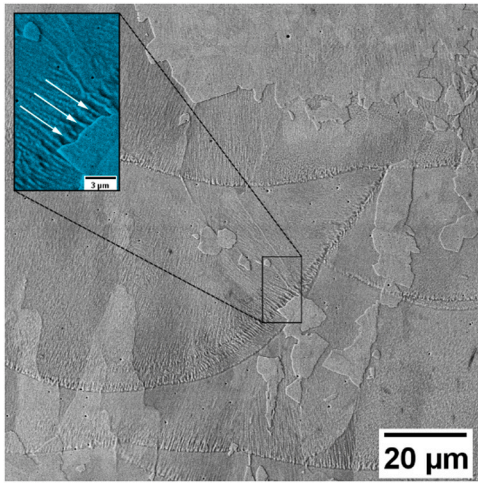


Fig. 13. SEM image of the cellular structures observed in the LPBF samples.

the martensitic transformation, favoring the back transformation $hcp-\epsilon \rightarrow fcc-\gamma$ and the accompanied strain recovery. The same effect might be achieved with the fine cellular structures. However, a more in-depth study on the interaction between the $hcp-\epsilon$ and the cell walls, e.g. by transmission electron microscopy (TEM), would be required, but is beyond the scope of the present work.

The high cost and the extreme sensitivity of functional properties of conventional Ni-Ti alloys on chemical composition, which cannot be very precisely controlled in the LPBF process, have partially restricted AM of SMAs. The present study demonstrates that Fe-Mn-Si SMAs are rather robust with regard to the influence of process-induced changes of the chemical composition on the shape memory properties. Indeed, although a 0.5 wt% loss of the volatile element Mn during the process was detected by EDX analysis, the alloy shape memory characteristics are not compromised. Therefore, LPBF can be identified as an attractive manufacturing option for the fabrication of inexpensive structures made of Fe-based SMAs. Furthermore, the pronounced variations in the functional properties of the investigated Fe-Mn-Si SMA resulting from changes in the generated microstructure and texture with AM processing conditions indicate the possibility of material's property control and optimization by intelligent manipulation of build parameters (e.g. laser parameters, build orientation). LPBF of Fe-based SMAs

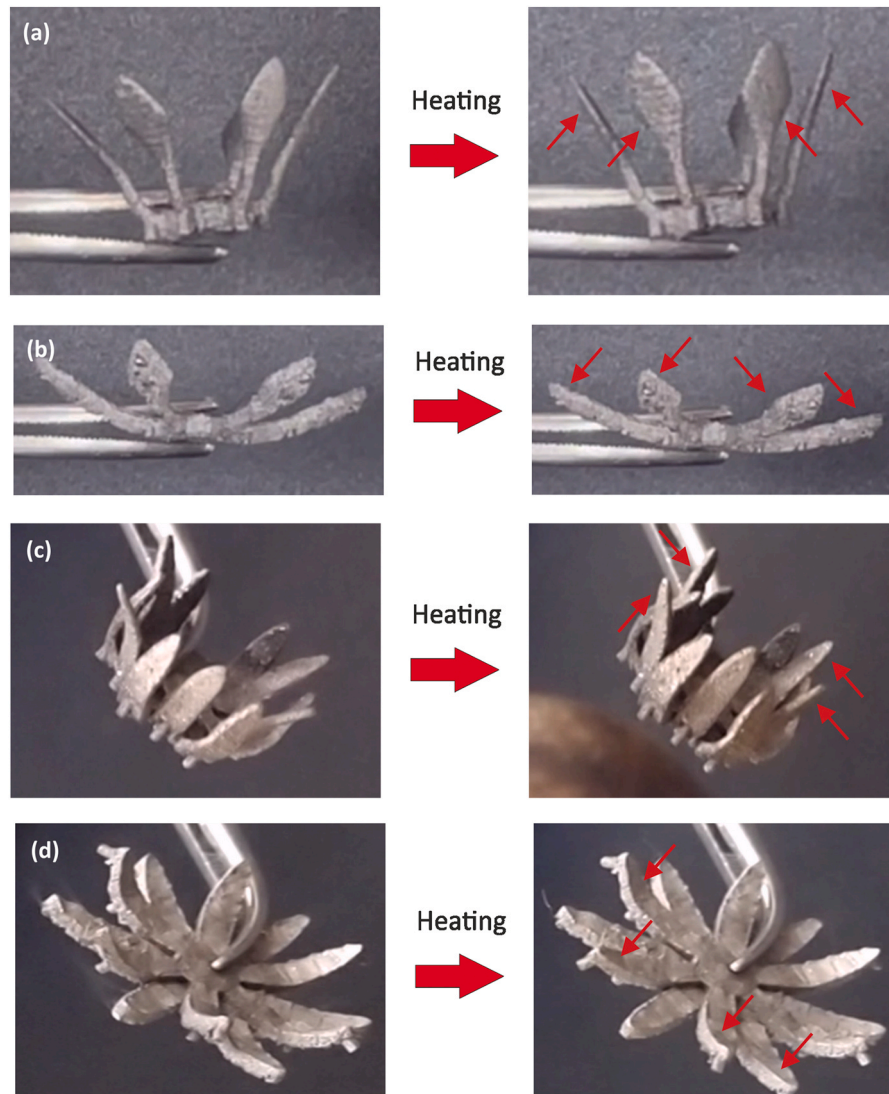


Fig. 14. (a,b) Shape changes of objects Type I upon heating to 300 °C after deformation; (c,d) shape changes of objects Type II upon heating to 300 °C after deformation.

provides new perspective for developing innovative cost-saving structures with tailored properties and functionalities.

5. Demonstration of complex 3D structure fabrication by LPBF

Complex structures with good dimensional accuracy and pronounced shape recovery were successfully produced by LPBF. The shape changes occurring after deformation and subsequent heating are shown in Fig. 14 (For more details, please refer to Movie S1, Supporting information) for two objects (Type I and Type II). Upon heating, a pronounced recovery of the originally printed shapes for every object tested is achieved and attributed to the back martensitic transformation.

Supplementary material related to this article can be found online at [doi:10.1016/j.addma.2021.102071](https://doi.org/10.1016/j.addma.2021.102071).

In addition to the possibility of texture and microstructure control described in the previous chapter, the design freedom associated with LPBF in comparison with conventional manufacturing techniques is also demonstrated. The pronounced SME observed in the complex objects produced for demonstration purposes underlines the high potential of LPBF for the fabrication of complex geometries. Actuators, lattice structures or structural metamaterials with optimized designs, which combine the SME of the Fe-based SMAs with additional structural and mechanical functionalities deriving from the specifically selected shape and topology, could be manufactured e.g. for damping applications.

6. Summary

In this study, the feasibility of fabricating bulk parts and complex-geometry structures by LPBF from a Fe–Mn–Si SMA was demonstrated for the first time. Parts characterized by high density and reduced amount of defects were manufactured with the selection of the optimal processing parameters. EBSD and XRD analysis were conducted in as-built and annealed samples to investigate the effect of processing parameters on phase and microstructure development. Thermo-mechanical behavior was characterized to correlate the final microstructure with shape memory properties. Several conclusions can be made:

1. A high VED (194.44 J/mm^3) was required in order to obtain high density and avoid lack of fusion defects. Only at high energy input, melting was sufficient to ensure good bonding among layers and tracks.
2. Processing parameters influenced the amount and distribution of different phases within the material due to variation in cooling rates. A significant reduction of the ferrite content as well as grain refinement were observed for high VED due to a solid-state transformation $\text{bcc-}\delta \rightarrow \text{fcc-}\gamma$ during cooling. Crack formation was also prevented with the reduced amount of $\text{bcc-}\delta$ in the final microstructure.
3. Samples produced with optimized parameters showed high strength and ductility, with fracture elongation up to 47.86% after heat treatment. Pronounced PE and SME were achieved in LPBF samples, with superior performance than specimens conventionally fabricated and containing VC precipitates.
4. Samples fabricated with loading direction parallel to the build direction showed more pronounced shape memory properties because of the increased amount of (101) grains, which are more prone for the phase transformation responsible for SME and PE.
5. The fabrication of Fe-based SMA by LPBF could be applied to complex structures with good dimensional accuracy. The printed complex-shaped objects demonstrated a pronounced shape recovery upon heating.

CRediT authorship contribution statement

Irene Ferretto: Conceptualization, Methodology, Validation, Investigation, Data curation, Visualization, Writing - original draft.

Dohyung Kim: Validation, Investigation. **Nicoló Maria Della Ventura:** Validation, Investigation, Writing - review & editing. **Moslem Shahverdi:** Validation, Writing - review & editing. **Wookjin Lee:** Conceptualization, Writing - review & editing, Supervision. **Christian Leinenbach:** Conceptualization, Writing - review & editing, Project administration, Supervision.

Declaration of Competing Interest

The authors declare that they have no known competing financial interests or personal relationships that could have appeared to influence the work reported in this paper.

Acknowledgment

The work is funded by the Swiss National Science Foundation (SNSF) through the project IZKSZ2_188290/1 and the National Research Foundation of Korea (NRF) under the grant number 2019K1A3A1A14065695, which is gratefully acknowledged.

Appendix A. Supporting information

Supplementary data associated with this article can be found in the online version at [doi:10.1016/j.addma.2021.102071](https://doi.org/10.1016/j.addma.2021.102071).

References

- [1] K. Ôtsuka, C.M. Wayman (Eds.), *Shape memory materials*, Cambridge University Press, Cambridge; New York, 1998.
- [2] A. Cladera, B. Weber, C. Leinenbach, C. Czaderski, M. Shahverdi, M. Motavalli, Iron-based shape memory alloys for civil engineering structures: an overview, *Constr. Build. Mater.* 63 (2014) 281–293, <https://doi.org/10.1016/j.conbuildmat.2014.04.032>.
- [3] L.C. Chang, T.A. Read, Plastic deformation and diffusionless phase changes in metals — the gold-cadmium beta phase, *JOM J. Miner. Met. Mater. Soc.* 3 (1951) 47–52, <https://doi.org/10.1007/BF03398954>.
- [4] W.J. Buehler, J.V. Gilfrich, R.C. Wiley, Effect of low-temperature phase changes on the mechanical properties of alloys near composition TiNi, *J. Appl. Phys.* 34 (1963) 1475–1477, <https://doi.org/10.1063/1.1729603>.
- [5] S. Saedi, N. Shayesteh Moghaddam, A. Amerinatanzi, M. Elahinia, H.E. Karaca, On the effects of selective laser melting process parameters on microstructure and thermomechanical response of Ni-rich NiTi, *Acta Mater.* 144 (2018) 552–560, <https://doi.org/10.1016/j.actamat.2017.10.072>.
- [6] L. Janke, C. Czaderski, M. Motavalli, J. Ruth, Applications of shape memory alloys in civil engineering structures—Overview, limits and new ideas, *Mat. Struct.* 38 (2005) 578–592, <https://doi.org/10.1007/BF02479550>.
- [7] M. Koster, W.J. Lee, M. Schwarzenberger, C. Leinenbach, Cyclic deformation and structural fatigue behavior of an Fe–Mn–Si shape memory alloy, *Mater. Sci. Eng. A* 637 (2015) 29–39, <https://doi.org/10.1016/j.msea.2015.04.028>.
- [8] M. Shahverdi, C. Czaderski, M. Motavalli, Iron-based shape memory alloys for prestressed near-surface mounted strengthening of reinforced concrete beams, *Constr. Build. Mater.* 112 (2016) 28–38, <https://doi.org/10.1016/j.conbuildmat.2016.02.174>.
- [9] M. Shahverdi, J. Michels, C. Czaderski, M. Motavalli, Iron-based shape memory alloy strips for strengthening RC members: material behavior and characterization, *Constr. Build. Mater.* 173 (2018) 586–599, <https://doi.org/10.1016/j.conbuildmat.2018.04.057>.
- [10] A. Sato, E. Chishima, K. Soma, T. Mori, Shape memory effect in $\gamma \rightleftharpoons \epsilon$ transformation in Fe–30Mn–1Si alloy single crystals, *Acta Metall.* 30 (1982) 1177–1183, [https://doi.org/10.1016/0001-6160\(82\)90011-6](https://doi.org/10.1016/0001-6160(82)90011-6).
- [11] C. Czaderski, M. Shahverdi, R. Brönnimann, C. Leinenbach, M. Motavalli, Feasibility of iron-based shape memory alloy strips for prestressed strengthening of concrete structures, *Constr. Build. Mater.* 56 (2014) 94–105, <https://doi.org/10.1016/j.conbuildmat.2014.01.069>.
- [12] C. Czaderski, B. Weber, M. Shahverdi, M. Motavalli, C. Leinenbach, W. Lee, R. Brönnimann, J. Michels, Iron-based shape memory alloys (Fe-SMA) - a new material for prestressing concrete structures, *Proceedings of SMAR 2015 the 3rd Conference on Smart Monitoring, Assessment and Rehabilitation of Civil Structures*. (2015) (12 pp.).
- [13] A. Arabi-Hashemi, W.J. Lee, C. Leinenbach, Recovery stress formation in FeMnSi based shape memory alloys: impact of precipitates, texture and grain size, *Mater. Des.* 139 (2018) 258–268, <https://doi.org/10.1016/j.matdes.2017.11.006>.
- [14] A. Arabi-Hashemi, E. Polatidis, M. Smid, T. Panzner, C. Leinenbach, Grain orientation dependence of the forward and reverse $\text{fcc} \leftrightarrow \text{hcp}$ transformation in FeMnSi-based shape memory alloys studied by in situ neutron diffraction, *Mater. Sci. Eng. A* 782 (2020), 139261, <https://doi.org/10.1016/j.msea.2020.139261>.
- [15] C. Leinenbach, A. Arabi-Hashemi, W.J. Lee, A. Lis, M. Sadegh-Ahmadi, S. Van Petegem, T. Panzner, H. Van Swyghoven, Characterization of the deformation

- and phase transformation behavior of VC-free and VC-containing FeMnSi-based shape memory alloys by in situ neutron diffraction, *Mater. Sci. Eng. A* 703 (2017) 314–323, <https://doi.org/10.1016/j.msea.2017.07.077>.
- [16] C. Leinenbach, H. Kramer, C. Bernhard, D. Eifler, Thermo-mechanical properties of an Fe–Mn–Si–Cr–Ni–VC shape memory alloy with low transformation temperature, *Adv. Eng. Mater.* 14 (2012) 62–67, <https://doi.org/10.1002/adem.201100129>.
- [17] L. Hitzler, J. Hirsch, B. Heine, M. Merkel, W. Hall, A. Öchsner, On the anisotropic mechanical properties of selective laser melted stainless steel, *Material* (2017), <https://doi.org/10.20944/preprints201708.0067.v1>.
- [18] M. Elahinia, N. Shayesteh Moghaddam, M. Taheri Andani, A. Amerinatanzi, B. A. Bimber, R.F. Hamilton, Fabrication of NiTi through additive manufacturing: a review, *Prog. Mater. Sci.* 83 (2016) 630–663, <https://doi.org/10.1016/j.pmatsci.2016.08.001>.
- [19] J. Van Humbeeck, Additive manufacturing of shape memory alloys, *Shap. Mem. Superelasticity* 4 (2018) 309–312, <https://doi.org/10.1007/s40830-018-0174-z>.
- [20] J.C. Chekutu, R. Groarke, K. O'Toole, D. Brabazon, Advances in selective laser melting of nitinol shape memory alloy part production, *Materials* 12 (2019) 809, <https://doi.org/10.3390/ma12050809>.
- [21] T. Bormann, N. Schumacher, B. Müller, M. Mertmann, M. de Wild, Tailoring selective laser melting process parameters for NiTi implants, *J. Mater. Eng. Perform.* 21 (2012) 2519–2524, <https://doi.org/10.1007/s11665-012-0318-9>.
- [22] C. Haberland, M. Elahinia, J.M. Walker, H. Meier, J. Frenzel, On the development of high quality NiTi shape memory and pseudoelastic parts by additive manufacturing, *Smart Mater. Struct.* 23 (2014), 104002, <https://doi.org/10.1088/0964-1726/23/10/104002>.
- [23] J. Frenzel, A. Wiecezorek, I. Opahle, B. Maaß, R. Drautz, G. Eggeler, On the effect of alloy composition on martensite start temperatures and latent heats in Ni–Ti-based shape memory alloys, *Acta Mater.* 90 (2015) 213–231, <https://doi.org/10.1016/j.actamat.2015.02.029>.
- [24] S. Saedi, N. Shayesteh Moghaddam, A. Amerinatanzi, M. Elahinia, H.E. Karaca, On the effects of selective laser melting process parameters on microstructure and thermomechanical response of Ni-rich NiTi, *Acta Mater.* 144 (2018) 552–560, <https://doi.org/10.1016/j.actamat.2017.10.072>.
- [25] T. Niendorf, F. Brenne, P. Krooß, M. Vollmer, J. Günther, D. Schwarze, H. Biermann, Microstructural evolution and functional properties of Fe–Mn–Al–Ni shape memory alloy processed by selective laser melting, *Met. Mater. Trans. A* 47 (2016) 2569–2573, <https://doi.org/10.1007/s11661-016-3412-z>.
- [26] F.C. Ewald, F. Brenne, T. Gustmann, M. Vollmer, P. Krooß, T. Niendorf, Laser powder bed fusion processing of Fe–Mn–Al–Ni shape memory alloy—on the effect of elevated platform temperatures, *Metals* 11 (2021) 185, <https://doi.org/10.3390/met11020185>.
- [27] J. Tian, P. Xu, J. Chen, Q. Liu, Microstructure and phase transformation behaviour of a Fe/Mn/Si/Cr/Ni alloy coating by laser cladding, *Opt. Lasers Eng.* 122 (2019) 97–104, <https://doi.org/10.1016/j.optlaseng.2019.06.003>.
- [28] P.X. Peng Xu, H.J. Heng Ju, C.L. Chengxin Lin, C.Z. Chaoyu Zhou, D.P. Dewei Pan, In-situ synthesis of Fe–Mn–Si–Cr–Ni shape memory alloy functional coating by laser cladding, *Chin. Opt. Lett.* 12 (2014) 041403–041405, <https://doi.org/10.3788/COL201412.041403>.
- [29] W.J. Lee, B. Weber, G. Feltrin, C. Czaderski, M. Motavalli, C. Leinenbach, Phase transformation behavior under uniaxial deformation of an Fe–Mn–Si–Cr–Ni–VC shape memory alloy, *Mater. Sci. Eng. A* 581 (2013) 1–7, <https://doi.org/10.1016/j.msea.2013.06.002>.
- [30] T. DebRoy, H.L. Wei, J.S. Zuback, T. Mukherjee, J.W. Elmer, J.O. Milewski, A. M. Beese, A. Wilson-Heid, A. De, W. Zhang, Additive manufacturing of metallic components – process, structure and properties, *Prog. Mater. Sci.* 92 (2018) 112–224, <https://doi.org/10.1016/j.pmatsci.2017.10.001>.
- [31] J.P. Oliveira, T.G. Santos, R.M. Miranda, Revisiting fundamental welding concepts to improve additive manufacturing: from theory to practice, *Prog. Mater. Sci.* 107 (2020), 100590, <https://doi.org/10.1016/j.pmatsci.2019.100590>.
- [32] Residual Stresses, Distortion, and Fatigue, in: *Welding Metallurgy*, John Wiley & Sons Ltd, 2002, pp. 122–141, <https://doi.org/10.1002/0471434027.ch5>.
- [33] Y.H. Wen, H.B. Peng, P.P. Sun, G. Liu, N. Li, A novel training-free cast Fe–18Mn–5.5Si–9.5Cr–4Ni shape memory alloy with lathy delta ferrite, *Scr. Mater.* 62 (2010) 55–58, <https://doi.org/10.1016/j.scriptamat.2009.10.004>.
- [34] N. Suutala, Effect of manganese and nitrogen on the solidification mode in austenitic stainless steel welds, *Met. Mater. Trans. A* 13 (1982) 2121–2130, <https://doi.org/10.1007/BF02648382>.
- [35] H. Peng, Y. Wen, Y. Du, J. Chen, Q. Yang, A new set of creq and nieq equations for predicting solidification modes of cast austenitic Fe–Mn–Si–Cr–Ni shape memory alloys, *Met. Mater. Trans. B* 45 (2014) 6–11, <https://doi.org/10.1007/s11663-013-0005-8>.
- [36] U. Scipioni Bertoli, G. Guss, S. Wu, M.J. Matthews, J.M. Schoenung, In-situ characterization of laser-powder interaction and cooling rates through high-speed imaging of powder bed fusion additive manufacturing, *Mater. Des.* 135 (2017) 385–396, <https://doi.org/10.1016/j.matdes.2017.09.044>.
- [37] M.J. Lai, Y.J. Li, L. Lillpopp, D. Ponge, S. Will, D. Raabe, On the origin of the improvement of shape memory effect by precipitating VC in Fe–Mn–Si-based shape memory alloys, *Acta Materialia* 155 (n.d.) 222–235.
- [38] S.H. Hong, Y.S. Han, The effects of deformation twins and strain-induced ϵ -martensite on mechanical properties of an Fe–32Mn–12Cr–0.4C cryogenic alloy, *Scr. Metall. Et. Mater.* 32 (1995) 1489–1494, [https://doi.org/10.1016/0956-716X\(95\)00193-Y](https://doi.org/10.1016/0956-716X(95)00193-Y).
- [39] A. Sato, E. Chishima, Y. Yamaji, T. Mori, Orientation and composition dependencies of shape memory effect IN Fe–Mn–Si alloys, *Acta Metall.* 32 (1984) 539–547, [https://doi.org/10.1016/0001-6160\(84\)90065-8](https://doi.org/10.1016/0001-6160(84)90065-8).
- [40] S. Kajiwar, Characteristic features of shape memory effect and related transformation behavior in Fe-based alloys, *Mater. Sci. Eng. A* 273–275 (1999) 67–88, [https://doi.org/10.1016/S0921-5093\(99\)00290-7](https://doi.org/10.1016/S0921-5093(99)00290-7).
- [41] N. Bergeon, G. Guenin, C. Esnouf, Microstructural analysis of the stress-induced ϵ martensite in a Fe–Mn–Si–Cr–Ni shape memory alloy: Part II: transformation reversibility, *Mater. Sci. Eng.: A* 242 (1998) 87–95, [https://doi.org/10.1016/S0921-5093\(97\)00512-1](https://doi.org/10.1016/S0921-5093(97)00512-1).